

SIMULATED X-RAY EMISSION FOR A RUNAWAY MODEL OF KEPLER’S SUPERNOVA REMNANT

PABLO F. VELÁZQUEZ

Instituto de Ciencias Nucleares, Universidad Nacional Autónoma de México, Apartado Postal 70-543, CP 04510,
México DF, Mexico; pablo@nucleares.unam.mx

CARLOS D. VIGH, ESTELA M. REYNOSO,¹ AND DANIEL O. GÓMEZ^{1,2}
Instituto de Astronomía y Física del Espacio, Ciudad Universitaria, C.C. 67, Sucursal 28, C.P. 1428,
Buenos Aires, Argentina; carlos@iafe.uba.ar, ereynoso@iafe.uba.ar, gomez@iafe.uba.ar

AND

E. MATÍAS SCHNEITER

Fysiska institutionen, Lunds Universitet, Box 118, SE-221 00, Sweden; mschneiter@gmail.com
Received 2006 February 1; accepted 2006 June 13

ABSTRACT

We present two-dimensional numerical simulations of a model for Kepler’s supernova remnant (SNR) carried out with the YGUAZÚ-A code. Following previous studies, we have assumed that the peculiar shape of this young remnant arises as a consequence of the interaction of the SNR blast wave with the bow shock formed by the wind of its high velocity progenitor. Furthermore, from our numerical results we have obtained synthetic X-ray emission maps, which can be directly compared with recent and previous observations of this SNR. Our models show that a nice fit with respect to the X-ray morphology and luminosity is obtained for a SN progenitor with mass-loss rate of $5 \times 10^{-5} M_{\odot} \text{ yr}^{-1}$, an ambient medium density of 10^{-2} cm^{-3} , an initial explosion energy of 8×10^{50} ergs, and a total ejected mass within $1.4\text{--}2.5 M_{\odot}$. In our simulations, parameters typical of a young population progenitor have not been considered. This model also predicts a $\sim 0.3\%$ yearly decrease in the total X-ray luminosity, which is consistent with observed values. The parameters employed in our runs correspond to a Type Ia supernova. Based on our simulations, we find that the expansion rate increases after the SNR blast wave overruns the bow shock, and we discuss whether this can explain the observed difference between the expansion rates measured from sequences of radio and X-ray images.

Subject headings: hydrodynamics — ISM: individual (Kepler SNR) — methods: numerical — shock waves — supernova remnants — X-rays: ISM

1. INTRODUCTION

Kepler’s supernova remnant (SNR) exploded 400 yr ago and is one of the few so-called historical SNRs. Both in radio and X-ray wavelengths, it appears as a circular $200''$ radius shell, brighter to the north and with two “ears” to the NW and SE. An emission band crosses the disk of the SNR from NW to SE, which might arise from material on the front and back sides of the shell seen in projection (Blair 2005). Combining Very Large Array (VLA) 6 and 20 cm observations, DeLaney et al. (2002) found variations of the spectral index around the remnant, with the steepest indices (~ -0.85) at the NW ear and the flattest ones (~ -0.65) at the northern bright arc. Spectral differences are also found in X-rays; while most of the X-ray emission is dominated by lines from Si, S, Ar, Ca, and Fe (Becker et al. 1980; Kinugasa & Tsunemi 1999), recent *XMM-Newton* (Cassam-Chenaï et al. 2004) and *Chandra* (Bamba et al. 2005) observations have revealed non-thermal thin filaments marking the outer edge of the SNR.

The distance to Kepler’s SNR is not well constrained; however, the most widely accepted value is ~ 5 kpc (Bandiera 1987; Reynoso & Goss 1999). The type of SN event is still not clear (see Blair 2005 for a review). While in recent years there was a general agreement in favor of a core-collapse event rather than a Type Ia, as was originally believed (Baade 1943), the abundances recently determined, based on *XMM-Newton* data (Cassam-Chenaï et al. 2004), can be indicative of a Type Ia event.

The expansion of Kepler’s SNR has been studied in different bands. In X-rays, Hughes (1999) found that the expansion time-scale and the true age of the SNR are coincident within the uncertainties, indicating that the shock front has undergone little or no deceleration. This result is in contrast with that obtained in the radio band, in which the SNR appears to be expanding as $R = t^{0.35}$ on the bright northern rim or as $R = t^{0.65}$ on the eastern part of the shell (Dickel et al. 1988). On the other hand, optical measurements yield velocities of the order of 100 km s^{-1} for compact knots (van den Bergh & Kamper 1977; Bandiera & van den Bergh 1991) and in the range of $2000\text{--}2500 \text{ km s}^{-1}$ for the northern non-radiative filaments (Sankrit et al. 2005). The optical knots are believed to correspond to circumstellar material ejected by the progenitor star prior to the SN outburst, which would therefore account for their low velocities. In addition, the expansion center of the optical knots was found to be moving away from the Galactic plane at a speed of $\sim 280 \text{ km s}^{-1}$ (Bandiera & van den Bergh 1991), a fact that accounts for the anomalous high Galactic latitude of the remnant ($6^{\circ}8$).

Images of Kepler’s SNR taken in radio, optical, or X-ray spectral ranges show a rather asymmetric structure, with its northern limb being much brighter than the rest of the remnant. This asymmetric brightness distribution has been associated with a density excess in the northern direction (D’Odorico et al. 1986). This overdense region also displays a spotlike distribution of matter, as indicated by the knots shown in optical images.

The pronounced asymmetry in brightness has been a matter of debate. The most likely explanation is that the SN shock front has evolved into a strong density gradient. However, high

¹ Member of the Carrera del Investigador Científico, CONICET.

² Also at Departamento de Física, Facultad de Ciencias Exactas y Naturales de la Universidad de Buenos Aires, Buenos Aires, Argentina.

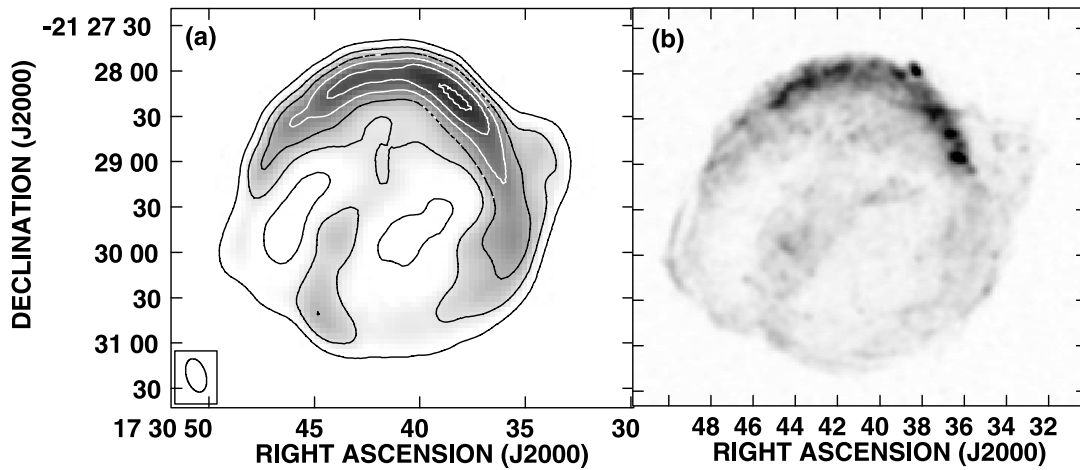


FIG. 1.—(a) Radio continuum image of Kepler’s SNR obtained with the VLA at 1.4 GHz (Reynoso & Goss 1999). The beam, 22.7×12.8 , P.A. = 17° , is indicated in the bottom left corner. (b) X-rays image of Kepler’s SNR obtained with *Chandra* in the range 2–10 keV.

densities are not expected as far away from the Galactic plane as Kepler’s SNR is located. One way to produce asymmetries in the density distribution is through an anisotropic stellar wind prior to the SN explosion (e.g., Jura et al. 2001). In the case of Kepler, even if the winds of the progenitor star were isotropic, the proper motion must have led to the formation of a bow shock (Bandiera 1987). The SNR shock front has overrun the bow shock, thus adopting the current asymmetrical morphology.

The main goal of the present paper is to quantitatively test the main features of the scenario proposed by Bandiera (also Borkowski et al. 1992) with the aid of numerical simulations. We perform two-dimensional (2D) axisymmetric simulations of the adaptive grid code YGUAZÚ-A in two stages: (1) the generation of the bow shock structure and (2) the expansion of the SNR in this environment. X-ray emission maps and spectra were obtained from numerical results, in order to perform a direct comparison with recent *Chandra* observations of this remnant.

The present manuscript is organized in the following way: in § 2 we describe the main features of Bandiera’s scenario; the initial conditions for numerical simulations and the overall features of the YGUAZÚ-A code are given in § 2.1; the simulation of the X-ray emission is discussed in § 2.2; the numerical results and comparison with observations are given in § 3; and finally, in § 4 we present our summary and conclusions.

2. DESCRIPTION OF THE MODEL

In Figure 1, we show images of Kepler’s SNR both in radio wavelengths (1.4 GHz; Reynoso & Goss 1999) and in X-rays. The latter, downloaded from *Chandra* Supernova Remnant Catalog, includes emission between 2.1 and 10 keV and is a smoothed version (using a Gaussian profile) of the raw data. Several lines are present in this spectral range. Both radio continuum and X-ray emission show a strong enhancement toward the NE direction.

Since Kepler’s SNR is located about 600 pc away from the Galactic disk, where the ISM is expected to be very tenuous, it is a challenging task to explain such an intense density gradient over a typical distance of only 2 pc. Bandiera (1987) presented an alternative and promising scenario to explain the asymmetry based on the following two assumptions: (1) Kepler’s progenitor had an intense stellar wind and (2) the progenitor had a fast proper motion with respect to the ISM in that region. A strong stellar wind (with typical mass-loss rates of early-type stars) would provide an overdense region in the surroundings of the progenitor, although not in an asymmetric fashion as it is observed. However, a fast

proper motion toward the northern direction would generate a bow-shock structure as a result of the collision between the supersonic (spherically symmetric) stellar wind and the supersonic uniform motion of the ISM observed in the star’s framework. This scenario is quite similar to the one assumed for comets. The main difference is that cometary flows are essentially adiabatic, while in this case radiative cooling plays a very important role (Huang & Weigert 1982).

According to Bandiera’s scenario, the overdense region in Kepler’s northern limb can be associated with the bow shock resulting from the collision of these two supersonic flows. The center of this bow shock is characterized by a stagnation point (zero velocity in the star’s reference frame), where the ram pressures of the stellar wind and the uniform flow of the ISM exactly balance each other. This stagnation point and the rest of the bow-shock structure, should move at the progenitor’s speed in the observer’s reference frame. Van den Bergh & Kamper (1977) studied the observed velocities of the optical knots present in the northern limb of Kepler’s SNR, and their results are consistent with a translational motion with no measurable signs of expansion, as expected from Bandiera’s scenario. However, Bandiera & van den Bergh (1991) reported some evidence (within 2.6σ) of expansion of these knots, with velocities between 40 and 90 km s^{-1} .

According to this scenario, the observed knots in the bow-shock region have been suggested to be the result of (1) the Kelvin-Helmholtz instability caused by the interstellar flow sliding tangentially through the external part of the shock and (2) thermal instabilities leading to the cooling and condensation of clumps surrounded by hotter and lighter plasma, while maintaining a pressure equilibrium.

When Kepler exploded 402 yr ago, it probably first expanded in the cavity blown by the stellar wind, with a typical density distribution $\rho \propto r^{-2}$, and it is currently reaching and energizing the bow shock. Even though the observed knots were formed before the SNR shock front reached and energized them, they have not yet been completely swept up by the corresponding contact discontinuity. Another possible origin for the observed knots would be the action of the Rayleigh-Taylor instability caused by the deceleration of the contact discontinuity of the SNR when hitting the overdense structure associated with the bow shock.

The main goal of the present paper is to quantitatively analyze the feasibility of this scenario by means of numerical simulations performed with the code YGUAZÚ-A. The technical features of

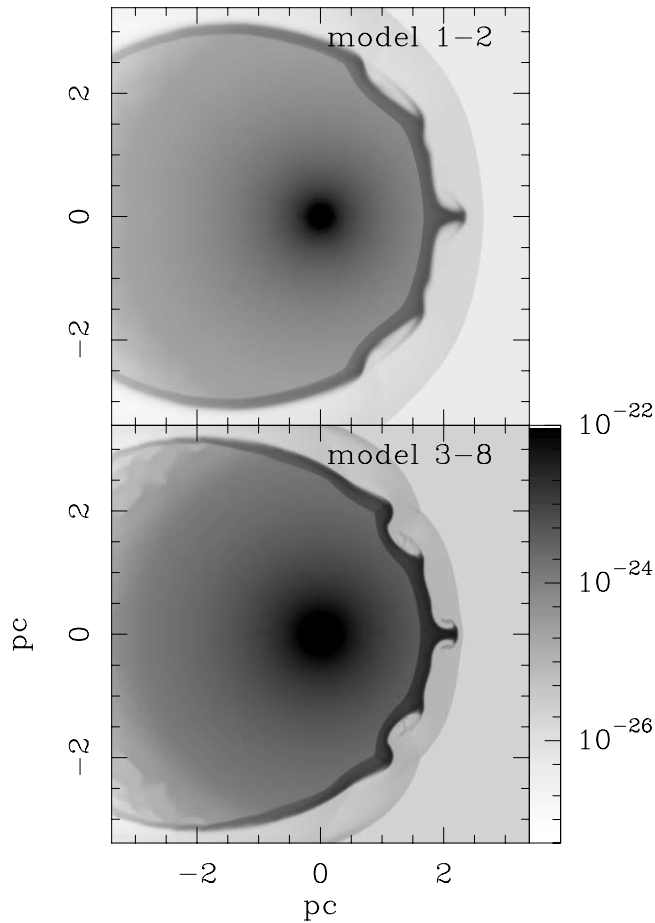


FIG. 3.—Density stratification of the bow shock (previous to the SN explosion) for models 1 and 2 (*top*) and 3–8 (*bottom*). The logarithmic gray scale is in units of g cm^{-3} . Vertical and horizontal axes are given in pc.

than 2 keV) but are practically negligible at higher energies. All these 1D models provide a partial hydrodynamic description for the evolution of SNRs but are clearly unable to explain the asymmetries shown by Kepler in both $\text{H}\alpha$ and X-ray images. Borkowski et al. (1994) carried out an X-ray spectrum study based on 2D numerical simulations reported by Borkowski et al. (1992), considering low overabundances in S, Si, and Fe.

The YGUAZÚ-A code only includes chemical species up to O IV (see § 2.1); hence, it is not possible to calculate a complete NEI X-ray emission coefficient from the simulations. Therefore, in order to compare our results with recent *Chandra* observations, we combined the T and n (temperature and electronic density, respectively) distributions obtained from our numerical results with a CHIANTI³ IEQ thermal X-ray emission model for the energy band 2–10 keV, which is a reasonable approximation according to Hughes & Helfand (1985). We computed the emission coefficient $j_\nu(n, T)$ over the energy band 2–10 keV using the CHIANTI atomic database and its associated IDL software (Dere et al. 1997; Landi et al. 2006), where the effects of the interstellar extinction (considering the extinction curve of Morrison & McCammon 1983) have been taken into account. Here we used the IEQ model developed by Mazzotta et al. (1998; also, Landini & Fossi 1991), where solar abundances were assumed with an excess in S and Si of 2.15 and 4.29, respectively.

³ Version 5.1 of the CHIANTI database and its associated IDL procedures are freely available at: <http://www.solar.nrl.navy.mil/chianti.html>, <http://www.arcetri.astro.it/science/chianti/chianti.html>, and <http://www.damtp.cam.ac.uk/users/astro/chianti/chianti.html>.

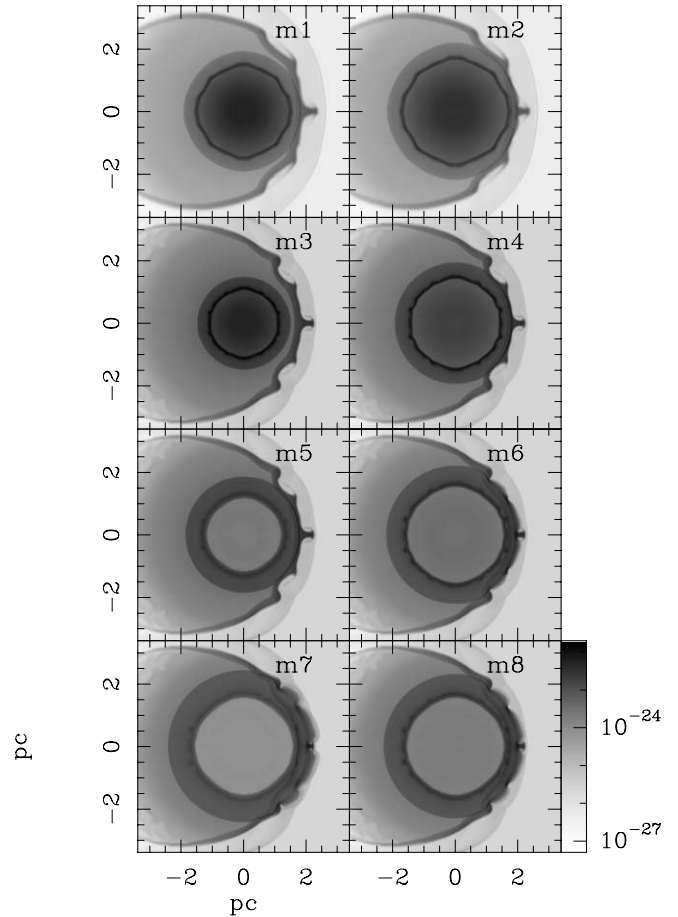


FIG. 4.—Density distribution at an integration time $t = 400$ yr, for all models.

3. RESULTS

3.1. Interacting Winds and SNR Evolution

As mentioned above, our numerical simulations have two stages: the first one consists of generating a cometary or bow-shock structure produced by the interaction of the isotropic stellar wind of the progenitor with the plane-parallel ISM wind and the second one is the evolution of a SNR expanding into this anisotropic medium.

The collision between the isotropic stellar wind and the plane-parallel ISM wind generates a bow-shock morphology. Figure 3 shows the initial (previous to the SN explosion) density distribution for models 1 and 2 (*top panel*) and 3–8 (*bottom panel*), where the stagnation point is located at 1.52 pc from the star position, which is consistent with equation (1). A double-shock structure is observed in Figure 3; it is formed by (1) a main shock or bow shock that sweeps up the incoming ISM wind and (2) the reverse shock which decelerates the stellar wind material. The shocked ISM and the stellar wind gas are separated by a contact discontinuity, located between the main and the reverse shocks. The reverse shock becomes radiative, and therefore the density of the internal part of the bow-shock structure increases. The wavy aspect present in the reverse shock is likely to arise as a consequence of thermal instabilities. The ISM density, n_0 , and the mass-loss rate, \dot{M}_5 , in models 3–8 is 5 times larger than in models 1 and 2 (see Table 1).

In this scenario, the SN explodes and its remnant evolves in a medium strongly modified by the stellar wind of its progenitor. The SNR shock wave expands in an environment with decreasing density ($\rho \propto r^{-2}$) until it reaches the bow shock structure.

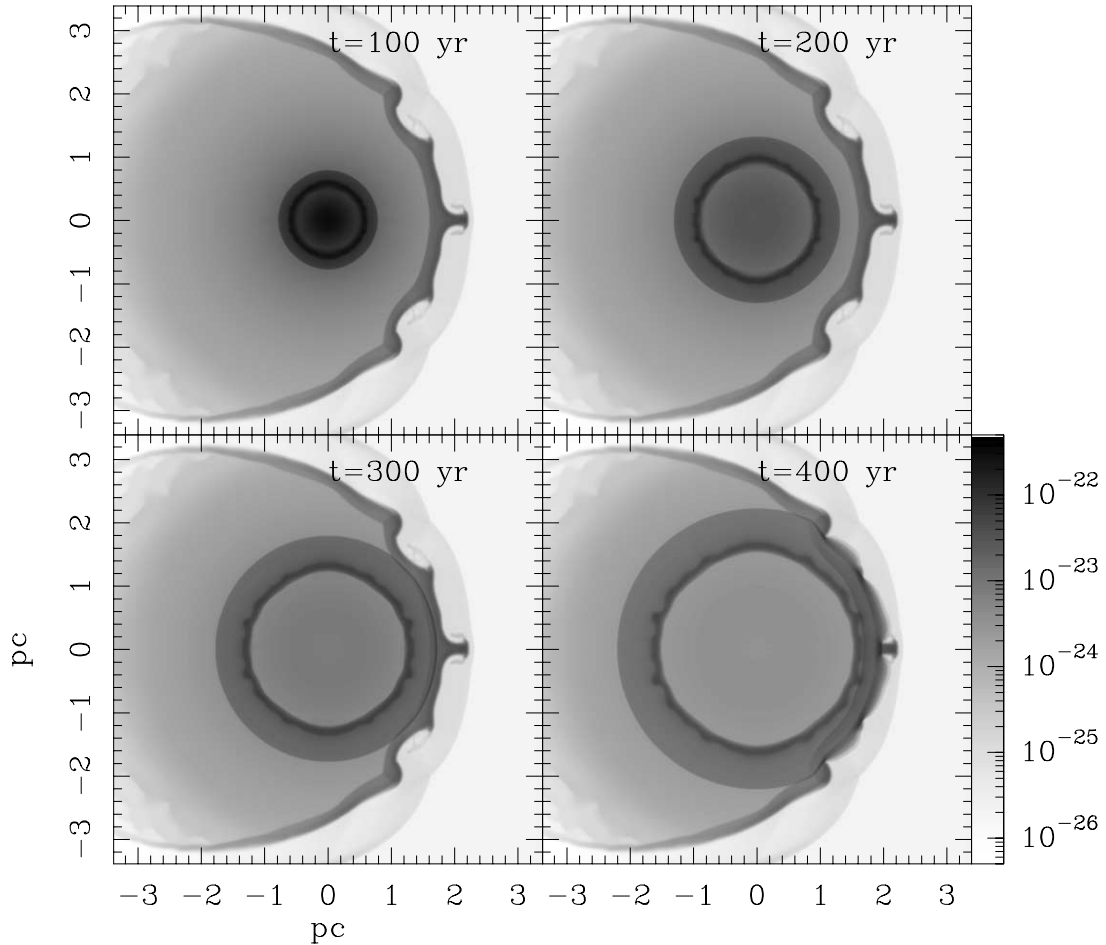


FIG. 5.—Density stratification of the interaction region between the SNR shock wave and the bow-shock structure at integration times of 100, 200, 300, and 400 yr for model 6.

Figure 4 is a comparison of the density distribution for all models at an integration time $t = 400$ yr. All maps, except model 3, show that the SN blast wave and the bow-shock structure are or have been interacting. Model 3 has an initial energy explosion $E_0 = 4 \times 10^{50}$ ergs and an ejected mass $M_* = 5 M_\odot$. The combination of a low E_0 and high M_* is responsible for the slow expansion. Maps corresponding to models 2 and 6–8 generate SNRs with radii of the order of 2 pc, which are similar to the radius observed for Kepler’s SNR (considering a distance of 5 kpc; Reynoso & Goss 1999).

The X-ray morphology and luminosity obtained for models 6–8 are comparable to the observed ones (this is further discussed in § 3.3); therefore, we select models 6–8 as the better candidates to explain the observed characteristics of Kepler’s SNR.

In order to study the evolution of the SNR–bow-shock interaction (shown in Fig. 5), the temporal evolution of the SNR density stratification for model 6 (models 7 and 8 behave similar to model 6) is integrated in the time range 100–400 yr. At early times, as long as $M_{\text{su}} \lesssim M_*$ (M_{su} is the stellar wind mass swept up by the SNR shock wave and M_* is the ejected mass), the temporal evolution of the SNR radius can be described as (Borkowski et al. 1992; Chevalier 1982)

$$R = r_0 \left(\frac{E_{51}^3}{M_5} \right)^{1/8} \left(\frac{v_{15}}{M_{-5}} \right)^{1/4} \left(\frac{t}{169 \text{ yr}} \right)^{3/4}, \quad (2)$$

where $M_5 = M_*/5 M_\odot$, $E_{51} = E_0/10^{51}$ ergs, and $r_0 = 1.52$ pc is the distance from the stagnation point to the star given by equa-

tion (1). At later times, when the interaction between the SN blast wave and the bow shock is in progress, this equation is no longer valid.

Equation (2) corresponds to a similarity solution that describes the interaction between stellar ejecta characterized by a power-law density profile, $\rho_{\text{ej}} \propto r^{-n}$, and the external medium (Chevalier 1982). The parameter n is related to the size of the SN progenitor. In our case $n = 6$, which corresponds to the relatively compact progenitor of a Type Ia SN (Borkowski et al. 1992). A comparison of equation (2) with our simulations at early times is a useful test of the compatibility between our code and these self-similar solutions. For instance, applying the parameters of model 6 to equation (2) at $t = 100$ yr, a SNR radius of 0.75 pc is obtained, very close to the radius of 0.77 pc given by our simulations (see Fig. 5).

Equation (2) is also useful for estimating the time at which the encounter between the SN blast wave and the bow shock will take place, at least in those cases for which $M_{\text{su}} \lesssim M_*$. For instance, this is the case for our model 3, since the swept-up mass and the ejected mass are equal at a distance of 1.5 pc from the SNR center, which is almost the distance to the stagnation point. The estimated collision time for model 3 is approximately 450 yr, which is larger than the age of Kepler’s SNR.

3.2. Expansion Rates

The expansion rate of a SNR can usually be approximated by a power law $R \propto t^m$, where R is its radius, t is its age, and m is the corresponding expansion parameter. In the case of Kepler, the

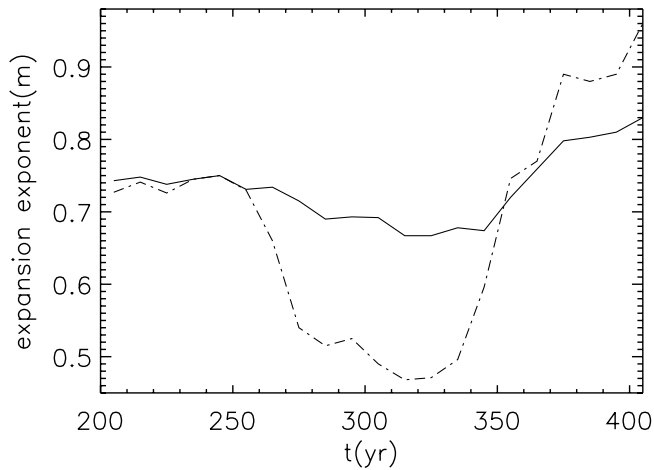


FIG. 6.—Temporal behavior of the average expansion parameters $\langle m \rangle$ (solid line) and m_i (dash-dotted line) for model 6, where $\langle m \rangle$ is the total expansion parameter and m_i represents the expansion in the direction of the stagnation point. These parameters were obtained considering time intervals of a decade for integration times between 200 and 400 yr.

mean expansion parameter $\langle m \rangle$ has been determined observationally to be $\langle m \rangle = 0.5$ (Dickel et al. 1988, based on radio continuum observations) and $\langle m \rangle = 0.93$ (Hughes 1999, comparing X-ray images from *ROSAT* and *Einstein*). Hughes (1999) suggests that this discrepancy indicates that the structures in the remnant giving rise to the X-ray emission have been decelerated considerably less than the radio-emitting structures. It is important to note that these observations were obtained during different time periods. Dickel et al. (1988) analyzed the Kepler expansion using VLA data observed between 1981 and 1985, while Hughes (1999) employed X-ray images from a wider temporal range, 1979–1981 (*Einstein*) and 1991–1997 (*ROSAT*).

We used our simulation data to generate images of Kepler at different integration times, in steps of 1 yr, in order to measure the temporal evolution of the expansion parameter $\langle m \rangle$ for model 6. We obtained $\langle m \rangle$ by comparing these images in time intervals of a decade, within the range 200–400 yr.

The results are given in Figure 6, where a comparison between the global expansion parameter $\langle m \rangle$ (solid line) and the expansion in the direction of the interaction region m_i (dash-dotted line) are plotted. An increase in the expansion rate of the remnant is observed in both cases.

During the interval 200–255 yr, both $\langle m \rangle$ and m_i remain close to 0.74, in reasonable agreement with Chevalier (1982; for the “ $n = 6$ ” case). The collision between the SNR and the bow-shock structure occurs at $t \simeq 275$ yr, observed in Figure 6 as a “dip” in both $\langle m \rangle$ and m_i , with a smaller minimum for m_i (dash-dotted line). For the Sedov solution, in the case where the SN explosion takes place in a circumstellar medium, a value of 0.66 is expected (Cavaliere & Messina 1976), which coincides with the minimum of $\langle m \rangle$. Nevertheless, as seen in the Figure 6, m_i (dash-dotted line) shows a more pronounced downfall reaching a minimum value of 0.47 which cannot be explained with the Sedov model. This behavior is a result of the interaction of the dense bow-shock structure with the SNR. Later, when the main SNR shock front has overrun the bow shock, the expansion rate suddenly grows, reaching values of $\langle m \rangle = 0.83$ and $m_i = 0.96$ at 400 yr. The latter value is in excellent agreement with the expansion parameter obtained by Hughes (1999). Furthermore, the minimum value $m_i = 0.47$ is close to the radio expansion parameter reported by Dickel et al. (1988).

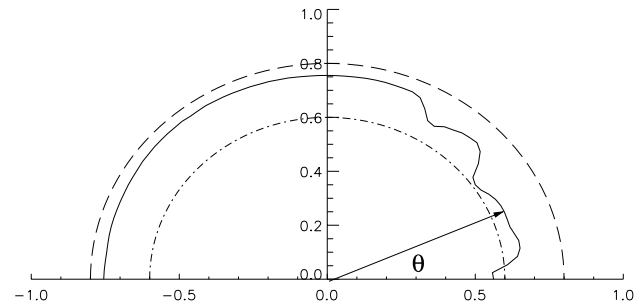


FIG. 7.—Polar graph of the expansion parameter vs. angle for model 6. The expansion was obtained considering integration times from 250 to 400 yr. A minor expansion rate of ~ 0.6 occurs at $\theta = 35^\circ$ and 57.5° , where θ is measured with respect to the direction of the stagnation point.

Figure 7 shows the expansion parameter as a function of θ , where θ is the azimuthal angle with respect to the stagnation point. The sites with lower expansion rates coincide with denser regions of the bow shock structure.

Therefore, our results provide an alternative explanation for the incompatibility between the expansion rates given by Dickel et al. (1988) and Hughes (1999); the observations might be describing different phases of the interaction between the SNR shock wave and the surrounding bow-shock structure. Although the time baselines involved in the observations (~ 10 yr between the second epoch data of each expansion measurement) are shorter than the theoretical time interval for the expansion parameter to increase from 0.46 to 0.96 (for m_i in the temporal range 325–400 yr, according to Fig. 6), we suggest that this hypothesis should remain open for further discussion. It would be helpful to analyze existing archival high-resolution radio continuum observations of Kepler’s SNR to investigate the trend followed by the expansion parameter since the last expansion measurement, which occurred about 20 yr ago. Besides, a deeper analysis of the model parameters may reveal if, under certain conditions, the measured difference (from $\langle m \rangle = 0.5$ to 0.93) can realistically occur within only 10 yr.

3.3. Simulated X-Ray Emission Maps

Figure 8 shows a comparison between the simulated X-ray emission maps of models 6 and 7 (top and bottom panels, respectively), at an integration time $t = 400$ yr (the age of Kepler’s SNR). In the left panels, we observe the simulated emission for the case $\phi = 0^\circ$, where ϕ represents the angle between the plane of the sky and the symmetry axis (given by the ISM wind velocity direction). Observationally, it is known that the star’s velocity forms an angle of 35° (Bandiera & van den Bergh 1991) with respect to the line of sight (i.e., 55° with respect to the plane of the sky). Hence, we also generated synthetic X-ray emission maps at $\phi = 55^\circ$ (right panels of Fig. 8).

In both models, an enhancement in X-ray emission is observed on the right side of the remnant shell for both projection angles ($\phi = 0^\circ$ and 55°). The annular structures are artifacts of the process of obtaining simulated maps from axisymmetric simulations. They appear when the clumps, produced by the collision between the shock and the dense shell formed behind the reverse shock, are projected all around the symmetry axis. Both models show a similar morphology, but the X-ray emission for model 7 is globally lower than that obtained for model 6.

The time evolution of the total X-ray luminosity L_X for model 6 is plotted in Figure 9. The luminosity L_X exhibits a local maximum

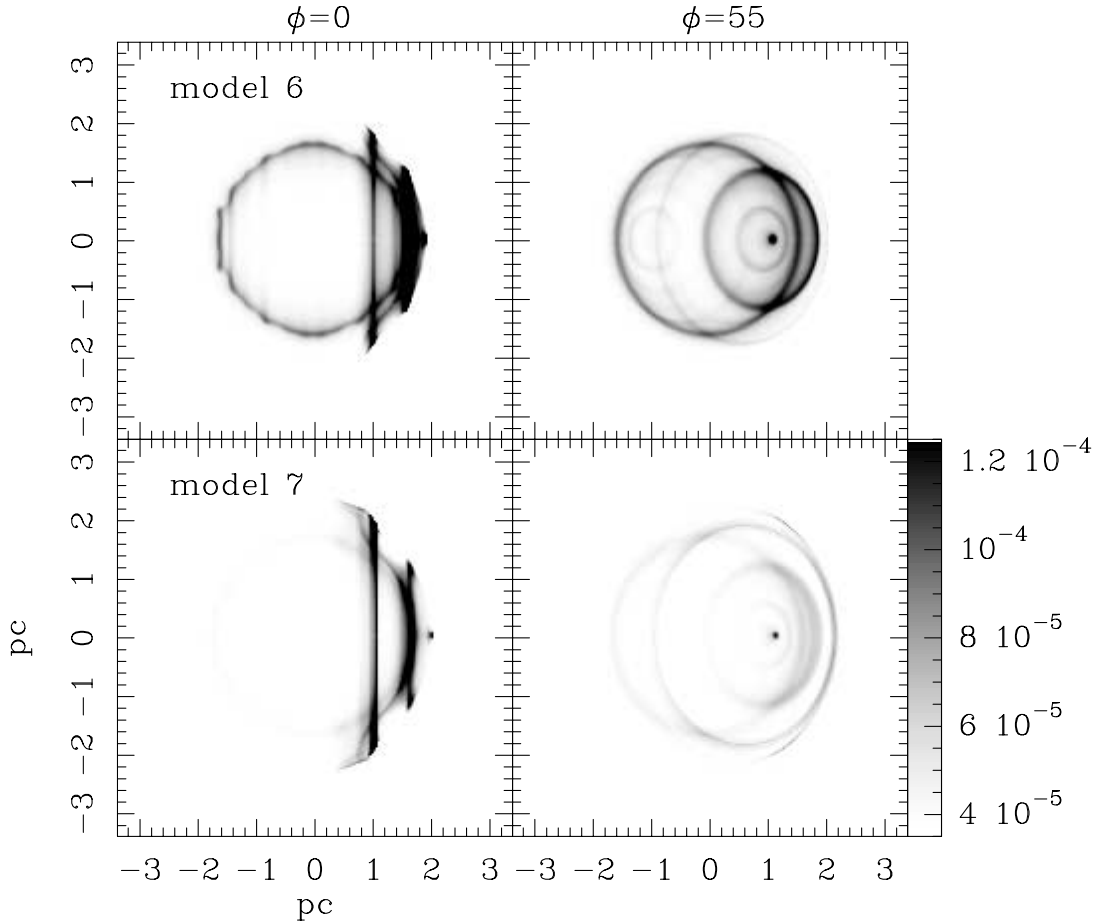


FIG. 8.—Comparison of the simulated X-ray emission maps for models 6 (top panels) and 7 (bottom panels). Left and right panels show $\phi = 0$ and $\phi = 55$ cases, respectively, where ϕ is the inclination between the symmetry axis and the plane of the sky.

at $t \sim 345$ yr which later decreases at a rate of 3% every 10 yr, in very good agreement with the observational results reported by Hughes (1999).

The synthetic spectrum obtained from model 6 is plotted in Figure 10. Several spectral lines are observed superimposed on

the continuum. These lines were identified by comparison with the spectrum presented in Figure 2 of Kinugasa & Tsunemi (1999), where the Si XIII $K\beta$, S XV $K\alpha$, and S XV $K\beta$ lines are observed in the energy interval 2–3 keV; lines corresponding to Ar XVII $K\alpha$ and Ca XIX $K\alpha$ are observed between 3 and 4 keV; and finally, the Fe-K blends are identified close to 6.4 keV.

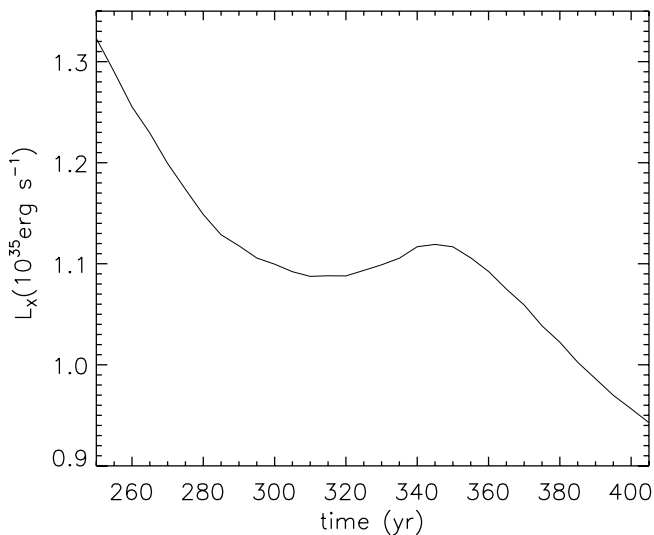


FIG. 9.—Plot of the total X-ray luminosity L_X vs. time (after the SN explosion) for model 6. After the collision of the SNR shock wave with the wind bow shock at $t \sim 290$ yr, a remarkable decrease in L_X is observed.

4. SUMMARY AND CONCLUSIONS

We present 2D axisymmetric numerical simulations to model the evolution of Kepler's SNR based on the scenario proposed by Bandiera (1987). Our simulations were carried out with the YGUAZÚ-A code. The simulations were carried out in two steps: (1) the interaction of the progenitor's stellar wind with the plane parallel ISM wind to form a bow-shock structure and (2) the propagation of the SNR in the anisotropic density structure formed in the previous step.

In order to make a direct comparison with recent *Chandra* observations, our numerical results were combined with the CHIANTI database to simulate X-ray emission maps and spectra in the 2–10 keV energy band. In these calculations an IEQ scheme was employed since the difference between the NEI and IEQ schemes is negligible for the energy band under consideration (Hughes & Helfand 1985).

Borkowski et al. (1992) carried out 2D numerical simulations based on Bandiera's scenario. In their work, the density distribution and the shape of the bow-shock structure were calculated analytically and this density distribution was used as an initial condition for their simulation. As a result, they concluded that

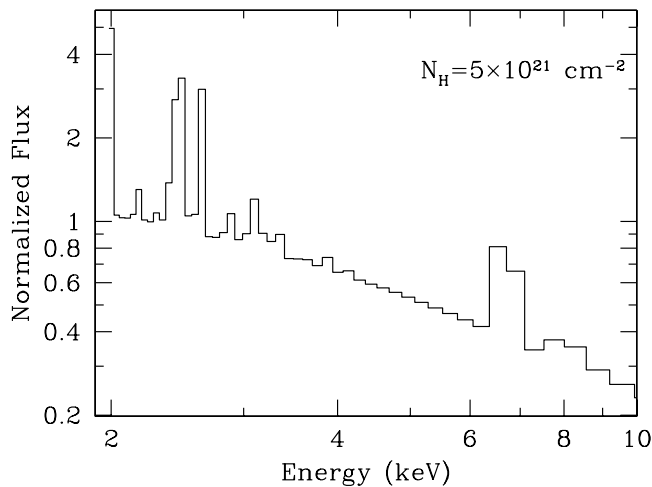


FIG. 10.—Synthetic X-ray spectrum for 2–10 keV energy band. For extinction calculations we use $N_{\text{H}} \approx 5 \times 10^{21} \text{ cm}^{-2}$. The intensity flux is normalized with respect to the maximum value of the continuum emission.

both the ISM density ($n_0 = 10^{-3} \text{ cm}^{-3}$) and the stellar mass-loss rate ($\dot{M} = 5 \times 10^{-6} M_{\odot} \text{ yr}^{-1}$) are lower than the one estimated by Bandiera (1987).

We quantitatively reexplored Bandiera’s scenario varying several input parameters, such as the initial energy explosion of the SN, the progenitor’s mass-loss rate, the progenitor’s stellar mass, and the unperturbed ISM density, in an attempt to reproduce several observational features, such as the overall morphology, X-ray spectra, and total X-ray luminosity, L_{X} , shown by *Chandra* observations.

In models (or runs) 1 and 2, we employed an ISM density n_0 and a mass-loss rate \dot{M} that are twice the values used by Borkowski et al. (1992). In spite of this, the X-ray luminosity corresponding to these runs are 1 order of magnitude lower than that observed. This result motivated us to try even higher values for n_0 and \dot{M} . For an integration time $t = 400 \text{ yr}$, runs 6–8 yield values for L_{X} and the X-ray emitting mass M_{X} of the order of the observational values (Table 2). The mass M_{X} is estimated considering the mass of gas with temperature higher than $2 \times 10^6 \text{ K}$. Dynamically, models 6–8 display a similar evolution to the one reported by Borkowski et al. (1992). However, in order to reproduce the observed X-ray luminosity, these models required mass-loss rates and interstellar densities about 1 order of magnitude higher than the ones used by Borkowski et al. (1992). Furthermore, model 6 shows a decrease in the total luminosity of the order of 3% every decade, which is comparable with the observational decreasing rate reported by Hughes (1999). Variations of the SN initial energy and progenitor’s stellar mass did not show any appreciable variation in the total luminosity (see Table 2).

Decourchelle & Ballet (1994) carried out 1D simulations of the evolution of Kepler’s SNR, exploring different scenarios in which Type Ia, Ib, and II events were considered. They found that the Type II assumption with no mass loss from the progenitor is able to reproduce the observed spectrum. On the other hand, Kinugasa & Tsunemi (1999) observed Kepler’s SNR using *ASCA* and found abundances consistent with a Type Ia SN explosion. The synthetic spectra obtained from our simulations, where a modest enhancement of Si and S typical of Type Ia events was used, are also in qualitative agreement with observations, reproducing several of the emission lines reported in Kinugasa & Tsunemi (1999).

TABLE 2
X-RAY LUMINOSITIES AND EMITTING MASS FOR DIFFERENT MODELS FOR AN INTEGRATION TIME OF 400 yr

PARAMETER	MODEL							
	M1	M2	M3	M4	M5	M6	M7	M8
$L_{\text{X}} (10^{34} \text{ ergs s}^{-1})$	0.5	0.7	7.3	11.0	6.4	9.5	7.5	8.6
$M_{\text{X}} (M_{\odot})$	3.3	3.8	7.4	9.4	5.9	8.3	7.5	8.0

Moreover, a Type Ia event is in agreement with the results found by Borkowski et al. (1994), who in addition assumed an Fe overabundance.

It is important to stress that our 2D simulations account not only for the spectrum but also for the size, morphology and total X-ray luminosity of the remnant. In particular, models 6–8 are the best candidates to explain the origin of Kepler’s SNR (see Figure 8). It is very hard to reproduce the morphology of this remnant without a combination of mass loss and high proper motion from the progenitor; therefore, we believe that our model provides a thorough explanation to the origin of this source.

Model 6 also predicts an increase in the expansion rate due to the passage of the SNR shock front through the bow shock. Radio and X-ray expansion measurements of Kepler’s SNR indeed yield very different values of the expansion parameter, with the earlier determination being almost half the value of the latest one. Note, however, that the predicted increase in the expansion parameter is not fast enough to quantitatively explain the reported difference. Analysis of high-resolution radio observations of Kepler during different epochs (which can be found in VLA archives), should confirm whether Kepler’s SNR is actually undergoing an increase in its global expansion or not.

As can be observed in Table 2, Figure 8, and Figure 10, the controversy about the characteristics of Kepler’s progenitor (for instance, its initial mass), is left as an open question. More observational and theoretical work is necessary to shed light on this issue.

In summary, our results confirm that Bandiera’s progenitor runaway model is a plausible scenario for explaining several observed features in Kepler’s SNR, such as its overall morphology (shown in X-ray and radio images), its X-ray spectra, or its total X-ray luminosity. Our results are also consistent with Kepler’s progenitor being a Type Ia SN (in agreement with Borkowski et al. 1992, 1994). However, higher ISM densities and mass-loss rates of the progenitor must be considered. These last conditions are in agreement with Bandiera (1987); although, he also considered young population progenitors with masses above $10 M_{\odot}$, which we do not explore here.

This work was supported by the CONACyT grants 41320-E, 43103-F, 46828-F, the DGAPA (UNAM) grant IN 113605, and partially financed by grants ANPCyT-14018 and UBACYT A055. The authors acknowledge an anonymous referee for her/his very useful comment which help us to improve a previous version of this manuscript. We thank Enrique Palacios, Martín Cruz, Israel Díaz, and Antonio Ramírez for computer support (ICN-UNAM) and Alberto Vásquez (IAFE) for his kind hospitality.

REFERENCES

- Baade, W. 1943, *ApJ*, 97, 119
- Badenes, C., Borkowski, K. J., & Bravo, E. 2005, *ApJ*, 624, 198
- Bamba, A., Yamazaki, R., Yoshida, T., Terasawa, T., & Koyama, K. 2005, *ApJ*, 621, 793
- Bandiera, R. 1987, *ApJ*, 319, 885
- Bandiera, R., van den Bergh, S. 1991, *ApJ*, 374, 186
- Becker, R. H., White, N. E., Boldt, E. A., Holt, S. S., & Serlemitsos, P. J. 1980, *ApJ*, 237, L77
- Blair, W. P. 2005, in *ASP Conf. Ser.* 342, 1604–2004: *Supernovae as Cosmological Lighthouses*, ed. M. Turatto et al. (San Francisco: ASP), 416
- Borkowski, K. J., Blondin, J. M., & Sarazin, C. L. 1992, *ApJ*, 400, 222
- Borkowski, K. J., Sarazin, C. L., & Blondin, J. M. 1994, *ApJ*, 429, 710
- Cassam-Chenaï, G., Decourchelle, A., Ballet, J., Hwang, U., Hughes, J. P., & Petre, R. 2004, *A&A*, 414, 545
- Cavaliere, A., & Messina, A. 1976, *ApJ*, 209, 424
- Chevalier, R. A. 1982, *ApJ*, 258, 790
- Decourchelle, A., & Ballet, J. 1994, *A&A*, 287, 206
- DeLaney, T., Koralesky, B., Rudnick, L., & Dickel, J. R. 2002, *ApJ*, 580, 914
- Dere, K. P., Landi, E., Mason, H. E., Monsignori Fossi, B. C., & Young, P. R. 1997, *A&AS*, 125, 149
- Dickel, J. R., Sault, R., Arendt, R. G., Korista, K. T., & Matsui, Y. 1988, *ApJ*, 330, 254
- D’Odorico, S., Bandiera, R., Danziger, J., & Focardi, P. 1986, *AJ*, 91, 1382
- Huang, R. Q., & Weigert, A. 1982, *A&A*, 116, 348
- Hughes, J. 1999, *ApJ*, 527, 298
- Hughes, J. P., & Helfand, D. J. 1985, *ApJ*, 291, 544
- Jura, M., Velusamy, T., & Werner, M. W. 2001, *ApJ*, 556, 408
- Kinugasa, K., & Tsunemi, H. 1999, *PASJ*, 51, 239
- Landi, E., Del Zanna, G., Young, P. R., Dere, K. P., Mason, H. E., & Landini, M. 2006, *ApJS*, 162, 261
- Landini, M., & Fossi, F. C. M. 1991, *A&AS*, 91, 183
- Mazzotta, P., Mazzitelli, G., Colafrancesco, S., & Vittorio, N. 1998, *A&AS*, 133, 403
- Morrison, R., & McCammon, D. 1983, *ApJ*, 270, 119
- Raga, A. C., de Gouveia Dal Pino, E. M., Noriega-Crespo, A., Mininni, P. D., & Velázquez, P. F. 2002, *A&A*, 392, 267
- Raga, A. C., Navarro-González, R., & Villagrán-Muniz, M. 2000, in *Rev. Mex. AA Ser. Conf.*, 36, 67
- Reynoso, E. M., & Goss, W. M. 1999, *AJ*, 118, 926
- Sankrit, R., Blair, W. P., DeLaney, T., Rudnick, L., Harrus, I. M., & Ennis, J. A. 2005, *Adv. Space Res.*, 35, 1027
- Sedov, L. I. 1959, *Similarity and Dimensional Methods in Mechanics* (New York: Academic Press)
- van den Bergh, S., & Kamper, K. W. 1977, *ApJ*, 218, 617
- van Leer, B. 1982, *Proc. 8th International Conf. on Numerical Methods in Fluid Dynamics*, ed. E. Krause (Berlin: Springer), 507